

# PSF ROTATION WITH CHANGING DEFOCUS AND APPLICATIONS TO 3D IMAGING FOR SPACE SITUATIONAL AWARENESS

Rakesh Kumar and Sudhakar Prasad

*Department of Physics and Astronomy, University of New Mexico, Albuquerque, NM 87131*

By exploiting the notion of orbital angular momentum of light beams, we have recently demonstrated a novel pupil-phase-engineered point-spread function (PSF) design in which as a function of defocus the PSF merely rotates without changing its shape materially over a considerable range of defocus values. Here we explore general properties of the rotating PSF design with respect to 3D imaging, including trade-offs between transverse and longitudinal resolutions. We also present the results of simulation of reconstruction of 3D scenes consisting of point sources from noisy image data based on this design.

## 1 Introduction

For a clear, well corrected imaging aperture in space, the point-spread function (PSF) in its Gaussian image plane has the conventional, diffraction-limited, tightly focused Airy form. Away from that plane, the PSF broadens rapidly, however, resulting in a loss of sensitivity and transverse resolution that makes such a traditional “best-optics” approach untenable for rapid 3D image acquisition. One must scan in focus to maintain high sensitivity and resolution as one acquires image data, slice by slice, from a 3D volume with reduced efficiency.

In this paper we describe a computational-imaging approach [1] to overcome this limitation. We propose the use of pupil-phase engineering to fashion a PSF that, although not as tight as the Airy spot, maintains its shape and size while rotating uniformly with changing defocus over many waves of defocus phase at the pupil edge. As one of us has shown recently [2], dividing a circular pupil aperture into  $L$  Fresnel zones, with the  $l$ th zone having an outer radius proportional to  $\sqrt{l}$ , and impressing a spiral phase profile of form  $l\phi$  on the light wave, where  $\phi$  is the azimuthal angle coordinate measured from a fixed  $x$  axis (the “dislocation” line) in the pupil plane, yields a PSF that rotates with defocus while keeping its shape and size.

Our PSF rotation concept is quite different from that employed by Piestun and collaborators [3] in which combine an appropriate selected subset of Gauss-Laguerre modes, followed by pupil-phase optimization, to create a double-helix rotating PSF pattern with high power throughput. This work preceded work by a different group [4] of a very similar flavor except that the double helix was dispensed with, by a different pupil-phase optimization strategy, in favor of a single-helix, or corkscrew, PSF. Much like the work presented here, because of its single-lobe structure the corkscrew PSF leads to less confusion in the image obtained for a relatively crowded field of point sources.

The present paper explores detailed properties of our rotating-PSF design, including a theoretical analysis of the trade-offs between transverse and longitudinal resolutions, simulation of image data for 3D scenes based on such a PSF and optimization based algorithms for their recovery, and more general design related issues. We shall derive an underlying conservation law that both controls the transverse-longitudinal trade-off and might suggest still more general design strategies with better rotational shape invariance.

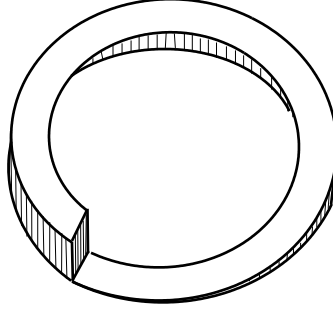
## 2 Rotating PSF Design

Consider a circular pupil of radius  $R$  that has been segmented into  $L$  different contiguous annular Fresnel zones, with the  $l$ th zone having an outer radius equal to  $R\sqrt{l/L}$ . The  $l$ th zone is endowed with a spiral phase profile of form  $l\phi$  that completes  $l$  complete phase cycles as the azimuthal angle  $\phi$  completes a single rotation about the optical axis, as shown in Figure 1. The phase dislocation lines for all the zones are taken to be a single fixed radial line, which we may take to be along the  $x$  axis in the pupil plane.

For such a phase encoded pupil, as a function of image-plane radial distance and azimuthal angle coordinates,  $s$  and  $\phi$ , the amplitude PSF  $K$  is given by the pupil integral

$$K(s, \phi; \zeta) = \frac{1}{\sqrt{\pi}} \int_{u \leq 1} d^2u \exp[i2\pi \vec{u} \cdot \vec{s} - i\zeta u^2 - i\psi(\vec{u})], \quad (1)$$

where  $\vec{s}$  is the image-plane position vector  $\vec{r}$  normalized by the in-focus diffraction spot-radius parameter at the imag-



n-turn spiral phase in the nth zone

Figure 1: Schematic diagram of a specific Fresnel zone with its spiral phase retardation

ing wavelength  $\lambda$  for the in-focus object plane a distance  $l_0$  from the pupil,

$$\vec{s} = \frac{\vec{r}}{r_0}, \quad r_0 \stackrel{\text{def}}{=} \frac{\lambda l_0}{R}, \quad (2)$$

and  $\vec{u}$  is the pupil-plane position vector  $\vec{\rho}$  normalized by the pupil radius,  $\vec{u} = \vec{\rho}/R$ . The defocus parameter  $\zeta$  is related to the object-plane distance  $\delta z$  from the in-focus object plane as

$$\zeta = \frac{\pi \delta z R^2}{\lambda l_0 (l_0 + \delta z)}. \quad (3)$$

In this scaled form, it is precisely equal to the phase at the edge of the pupil that results from the actual spatial defocus. The incoherent PSF,  $h(s, \phi; \zeta) = |K(s, \phi; \zeta)|^2$ , is normalized to have area 1, corresponding to a clear aperture that transmits all the light falling on it.

For the Fresnel-zone spiral phase function  $\psi(u, \phi_u)$  discussed above, we may evaluate the integral (1) as

$$\begin{aligned} K(s, \phi; \zeta) &= \frac{2\pi}{\sqrt{\pi}} \sum_{l=1}^L i^l \exp(il\phi) \\ &\times \int_{\sqrt{(l-1)/L}}^{\sqrt{l/L}} du u J_l(2\pi u s) \exp(-i\zeta u^2), \end{aligned} \quad (4)$$

where we used the identity

$$\oint d\phi_u \exp[ix \cos(\phi_u - \phi) + il(\phi_u - \phi)] = 2\pi i^l J_l(x) \quad (5)$$

in which integration is performed over a fundamental period of the azimuthal angle  $\phi_u$ . For sufficiently small  $s$  the integration over  $u$  may be performed approximately by treating the Bessel function  $J_l$  as a constant over the  $l$ th zone. Such an evaluation reveals the approximate rotational character of the PSF with changing defocus,

$$\begin{aligned} K(s, \phi; \zeta) &\approx 2\sqrt{\pi} \exp[i\zeta/(2L)] \frac{\sin[\zeta/(2L)]}{\zeta} \\ &\times \sum_{l=1}^L i^l \exp[i l(\phi - \zeta/L)] J_l(2\pi \sqrt{l/L} s). \end{aligned} \quad (6)$$

The prefactor in this expression also indicates that the PSF must break apart for values of  $|\zeta|$  outside the range  $(-L\pi, L\pi)$  over which the PSF performs one complete rotation. These properties of the PSF are easily verified by means of the numerically evaluated exact expression [2].

### 3 A Conservation Law

Allowing PSF to rotate with defocus stabilizes its shape, much as a spinning mechanical gyroscope resists changes of its rotational state. While the mechanical analogy is suggestive, it must be substantiated by any equations governing the PSF behavior in the face of a changing defocus. A particularly useful equation is that obeyed by the amplitude PSF  $K$ ,

$$i \frac{\partial K}{\partial \zeta} = -\frac{1}{4\pi^2} \nabla^2 K, \quad (7)$$

which is easily verified from the integral expression (1) for  $K$ . Here  $\vec{\nabla}$  denotes the two-dimensional gradient operator in the image plane. Equation (7) is formally identical to the Schrödinger equation of motion for the wavefunction of a free particle in quantum mechanics (QM). It therefore admits a simple conservation law for the intensity PSF,  $h = |K|^2$ , rather analogous to the probability flux conservation law in QM,

$$\frac{\partial h}{\partial \zeta} = -\frac{1}{4\pi^2 i} \vec{\nabla} \cdot (K^* \vec{\nabla} K - K \vec{\nabla} K^*), \quad (8)$$

which may be expressed more simply in terms of  $h$  and the phase of  $K$ , namely  $\Psi_K$ , by substituting  $K = \sqrt{h} \exp(i\Psi_K)$ ,

$$\begin{aligned} \frac{\partial h}{\partial \zeta} &= -\frac{1}{2\pi^2} [\vec{\nabla} h \cdot \vec{\nabla} \Psi_K + h \nabla^2 \Psi_K] \\ &= -\frac{1}{2\pi^2} \vec{\nabla} \cdot (h \vec{\nabla} \Psi_K). \end{aligned} \quad (9)$$

This last expression may be made more suggestive by transforming it, via the divergence theorem, into an integral form over any domain  $D$  bounded by the closed curve  $C$  in the image plane

$$\frac{d}{d\zeta} \iint_D h \, d^2r = -\frac{1}{2\pi^2} \oint_C h \frac{\partial \Psi_K}{\partial n} dl, \quad (10)$$

in which the vector field  $h \vec{\nabla} \Psi_K$  represents a kind of boundary probability-flux density per unit cross-length that determines what fraction of the PSF is lost from  $D$  through  $C$ .

The conservation law (10) contains the essence of why adding rotation might stabilise the PSF against spreading. For the PSF (6), the flux density vector  $h \vec{\nabla} \Psi_K$  is dominated by its azimuthal component, proportional to  $\partial \Psi_K / \partial \phi$ , for which the PSF merely circulates without spreading as the defocus  $\zeta$  is varied. In fact, one might want to calculate the fraction of the PSF area that is contained inside an azimuthally rotating domain with suitably chosen angular velocity  $\omega$  rad/defocus by transforming to the rotating frame of the PSF. The evolution of the PSF area contained in such a rotating domain is sensitive to only differential rotations between different parts of the PSF and to any residual, diffusive radial spreading, as described by Eq. (9).

### 4 Numerical Results for PSF Rotation

Figure 2 shows the PSF rotation with defocus [2] for the case of 7 Fresnel zones,  $L = 7$ . The surface plot of  $|K|^2$ , with  $K$  given by expression (4), is made at a succession of increasing values of the defocus parameter  $\zeta$ . While the PSF remains nearly shape and size invariant as it rotates at the rate of  $1/L$  radians per unit defocus phase completing a full rotation for a defocus change of about  $2\pi L$  radians, in consistency with the approximate result (6), there is clear evidence of differential rotation and slow spreading. The secondary lobe of the PSF clearly lags the main lobe even as the latter shears under such differential rotation. After a complete rotation the PSF begins to show rapid break-up and spreading, presaged by the  $\zeta$ -dependent sine prefactor in the approximate expression (6). But over the same range of defocus values from  $-24$  rad to  $24$  rad, the ideal diffraction-limited (IDL) PSF exhibits no rotation but a rapid spreading away from zero defocus, as is well known and shown in the bottom panel of plots.

We now give a physically appealing explanation of the origin of PSF rotation. A nonzero defocus of a point source means a quadratic optical phase in the pupil that, because of the square-root dependence of the zone radius on the zone number, increases on average by the same amount from one zone to the next. This uniformly incrementing phase yields, in effect, a rotation of the phase dislocation line, and thus a rotated PSF. Since the zone-to-zone phase

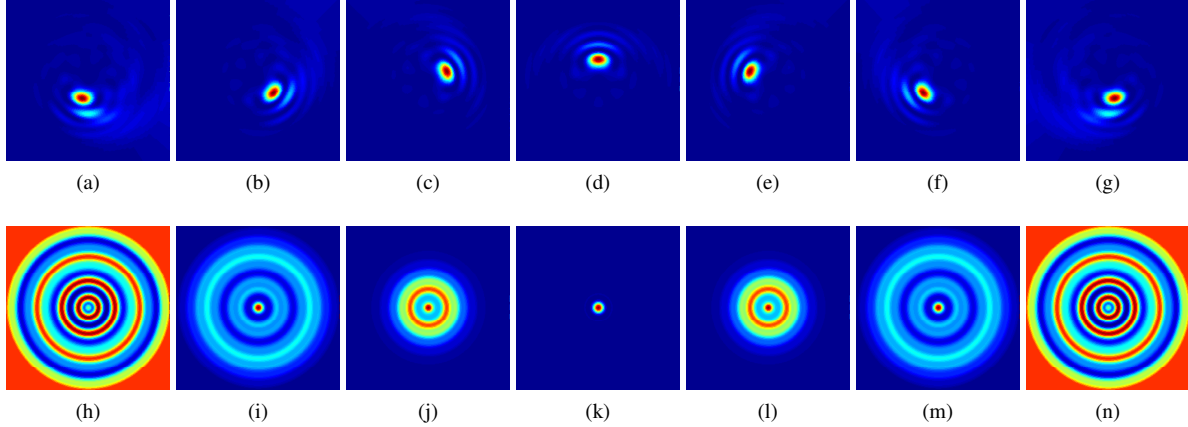


Figure 2: Surface plots of the incoherent rotating PSF, with  $L = 7$  zones (top row) in the Fresnel-zone partitioning of the pupil. The IDL-PSF is shown in the bottom row of plots. The plots from left to right are for increasing values of defocus, namely  $-24, -16, -8, 0, 8, 16,$  and  $24$  radians at the pupil edge.

increment depends linearly on defocus to first order, the PSF rotates uniformly with changing defocus to that order. The breakdown of this first-order approximation occurs slowly over a complete rotation of the PSF, corresponding to a change of about  $2\pi L$  radians of defocus phase at the pupil edge.

## 5 Three-Dimensional Image Data and Parameter Recovery via Rotating PSF

The shape and size invariance of the rotating PSF should allow rapid acquisition of a full three-dimensional (3D) image scene with high sensitivity, at least within the large range of defocus values over which such invariance holds approximately. In fact, for an image field consisting of point sources that are not too crowded, it should permit an efficient recovery of their full three-dimensional coordinates. Our recent simulations of reconstructions from image data for 3D image scenes comprised of point sources at different focal depths have shown remarkable robustness of the rotating-PSF approach to achieve good transverse and longitudinal resolution even for moderate SNR.

### 5.1 Reconstruction of Point Sources

We ran a number of simulation-based tests for the extraction of source parameters from a 3D scene known to consist of point sources alone. For this case, the simplest inverse problem one can set up to extract the number of point sources and their spatial coordinates and flux is that of minimizing the following unregularized cost function:

$$C(\{\mathbf{r}_1, \dots, \mathbf{r}_P; z_1, \dots, z_P; F_1, \dots, F_P\}) = \frac{1}{2\sigma^2} \|\mathbf{G} - \sum_{i=1}^P F_i \mathbf{H}(\mathbf{r}_i; z_i)\|_2^2, \quad (11)$$

where  $\mathbf{G}$  denotes the two-dimensional noisy image data matrix,  $\mathbf{H}(\mathbf{r}_i; z_i)$  the rotating PSF (blur) matrix for the  $i$ th point source of flux  $F_i$ , transverse location  $\mathbf{r}_i$ , and depth  $z_i$ . The number of sources,  $P$ , is not known *a priori* but is to be estimated from the data themselves. The minimization of (11) is performed iteratively until agreement with noise is attained, roughly when the average  $\chi^2$ -value equal to the number of image-plane pixels is reached. Much as in Ref. [5], the procedure is repeated for different values of  $P$  starting from 1 until the minimum value of the cost function is consistent with the mean  $\chi^2$  value.

The starting guesses of the point-source locations, particularly in the transverse image plane, are dictated by the spatial distribution of the image data. They must be chosen to allow for spatial overlap between the estimate computed from the forward model based on these locations and the image data to induce the optimization algorithm to move the estimate down the cost-function landscape in the space of the parameters being estimated. All the source fluxes were started at zero value as were all the depth coordinates.

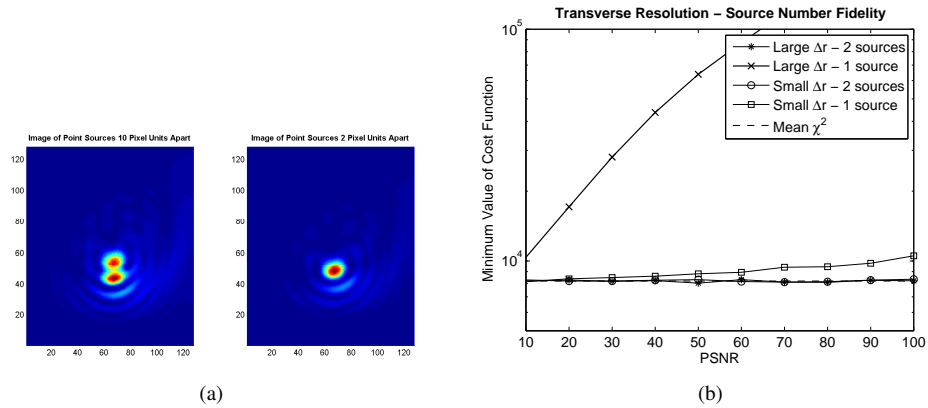


Figure 3: (a) Image of the point-source pair for the two different source separations of 10 and 2 pixel units. The two sources were taken to be in the same defocused depth plane, corresponding to a defocus phase at the pupil edge of 10 radians. (b) Minimum value of the cost function achieved by the algorithm vs. PSNR, for two different source separations. The mean  $\chi^2$  value of  $N_p^2/2$  is shown by the dashed line.

We now present the results of our simulation of the problem of resolving two point sources that are either at the same depth but differing transverse locations or at the same transverse location and different depths (*i.e.*, along the “line of sight”), for varying levels of detection noise, distributed normally in an (independent and identically distributed) IID fashion across the image pixel array. The purpose of this exercise was to set practical sensitivity limits on transverse and longitudinal resolutions for our computational 3D imager.

In Figure 3(b), we show as a function of the peak SNR (PSNR) the minimum value of the cost function (11) that the optimizer, *fminunc*, was able to drive down toward the mean  $\chi^2$ -value for “perfect” fit, which is  $N_p^2/2$  for an  $N_p \times N_p$  image. Since in the presence of noise the cost function can fluctuate around its mean value by amount of order  $\sigma_\chi = N_p/\sqrt{2}$ , of order 90 for  $N_p = 128$  used in our simulations, we expect the agreement for a “perfect” fit between the actual data and the forward-model-based data estimate to be within 1-2 times  $\sigma_\chi$ . For two sources to be considered “resolved,” we must be able to demonstrate that starting with either one or three-source guesses cannot reduce the cost function down to  $N_p^2$  at these SNR values, regardless of how they are chosen initially. The first two plotted curves represent the cases of two different values, namely 1 and 2, for the number of point sources. The two point sources in the actual image were taken to be 10 pixel units apart but in the same depth plane corresponding to 10 radians of defocus phase at the pupil edge. Since the main lobe of the PSF is about 10 pixel units across its short axis along which the sources are separated, this scenario corresponds to minimally-resolved point sources. Not surprisingly, the one-source assumption is completely untenable here, as seen in its high minimum value of the cost function at all of these PSNR values. While not shown, the three-source assumption does seem to attain the  $\chi$ -squared fit, but a careful examination of the recovered parameter values revealed that one of the three sources had vanishing flux, consistent in effect with a two-source assumption after all.

When we bring the point sources closer, placing them only 2 units apart along the short dimension of the PSF, so their noise-free images overlap considerably, as shown in Figure 3(a). These sources may be regarded as being barely, if at all, resolvable. In this case both the one-source and two-source starting guesses seem to produce comparable cost-function minima, as we see from the third and fourth plots in Figure 3(b), although the rise of the curve for the one-source guess above the curve for the correct two-source guess with increasing PSNR indicates that the sources can be resolved at sufficiently high values of the PSNR. The ability to achieve arbitrary amounts of spatial resolution depends on the SNR, as is well known from a number of early works [6], a fact confirmed by the present paper as well. The number of iterations to achieve the minimum value of the cost function in all cases turned out to be around 50.

Our conclusions are illustrated more directly by considering a scatter plot of the reconstructed positions of the point sources. We plot in Figure 4 the  $x, y$  coordinates of the estimates for the same values of PSNR for the two cases of resolvable and non-resolvable pairs of point sources considered in the previous figures. The reconstructed positions of the two point sources are given an extension inversely proportional to the PSNR value of the reconstruction, so, *e.g.*, a tight spot represents a high-PSNR estimate. It is clear from this figure that in the former case, the two sources

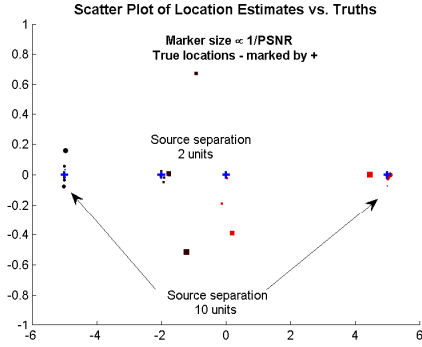


Figure 4: Estimated positions of the two point sources in the two cases of large and small transverse separations, with round spots for the former case and square spots for the latter case. The scatter plot shows excellent position estimate in the former case, but poorer agreement with the true positions in the latter case except at the highest few values of the PSNR considered.

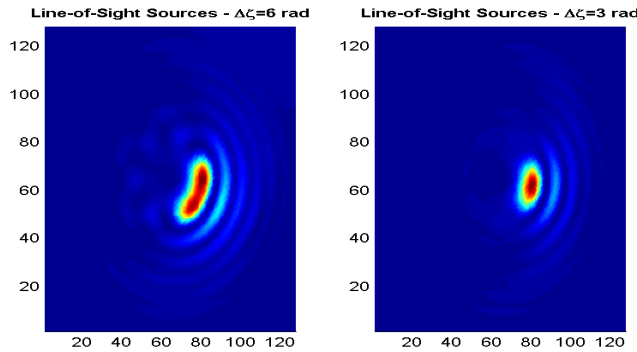


Figure 5: Image of the point-source pair in the line of sight at the center of the field but at two different depths, corresponding to (a) 0 and 6 radians and (b) 0 and 3 radians of defocus phase at the pupil edge.

are indeed well resolved tightly around their true positions even at the lowest PSNR of 10, while in the latter case, the scatter of reconstructed position is dramatically larger than their true separation except for the highest few PSNR values, signaling a barely resolved binary source.

We next explored the question of longitudinal, or depth ( $z$ ), resolution for two point sources that are along the same line of sight but at slightly different depths, as measured by the defocus phase at the pupil edge of value 6 radians and 3 radians, for the two images shown in Figure 5. The first case, as one may appreciate, corresponds to  $z$ -resolvable sources, while in the latter case the sources seem visually irresolvable. Yet, our analysis of depth estimates shows that in both cases the depth estimates are quite accurate. This is shown in Figure 6(a) where the estimates are shown as a function of the PSNR. The true defocus phases of 0, 6, 0, and 3 radians are shown by the dashed lines on this plot. This is supported by the observation that the minimum value of the cost function is well within  $\pm 2\sigma$  of the mean  $\chi^2$  value of  $N_p^2/2$  for both cases when the correct two-source assumption is made in the reconstruction. For the incorrect one-source assumption, the minimum value of the cost function in both cases is well outside this range of “fit” to data within the noise. Figure 6(b) shows the minimum cost function for the same ten PSNR values discussed earlier for the correct two-source assumption and the incorrect one-source assumption in the two cases.

The problem of recovering the location and flux parameters of a 3D scene consisting of  $P$  point sources alone requires optimization in a low-dimensional parametric space of dimensionality  $4P$ . This is a relatively simple problem with high sparsity, a fact that is responsible for a highly robust reconstruction protocol that may even yield some degree of superresolution, as we have seen above. The reconstruction is a lot more complicated and far less noise-robust, however, when an extended 3D source of continuously varying depth profile across the field is imaged with a

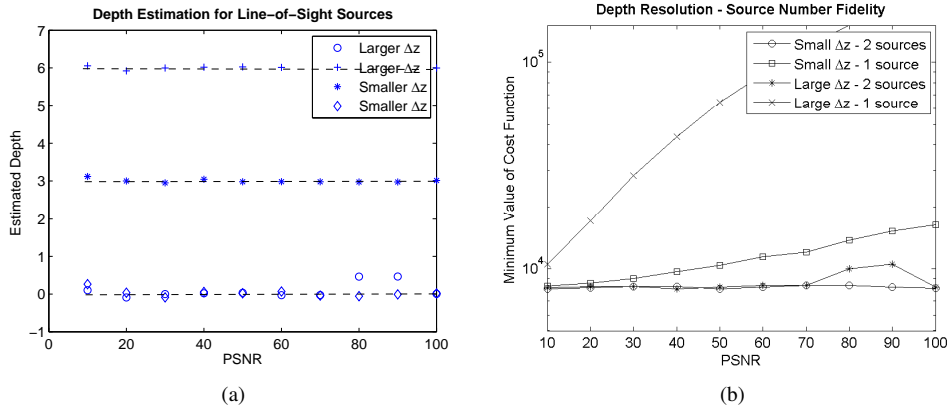


Figure 6: (a) Estimated defocus phases for the two point sources and (b) minimum value of the cost function achieved by the algorithm vs. PSNR for the same two cases as in Fig. 6. In (a), the dashed lines are drawn at the correct defocus phases.

rotating-PSF imager. It is to this problem that we briefly turn next and describe our preliminary results.

## 5.2 Extended 3D Sources and Two-Frame Reconstruction

Generalizing our 3D imaging and recovery of scenes consisting of point sources alone to extended sources is highly nontrivial. That is because point sources can be represented exactly in terms of a small number of parameters, which provides a very tight constraint on image-data inversion even in the presence of considerable amounts of noise. For an extended 3D object, the full description, even for a single pose of the object, requires the specification of both the brightness and depth, namely  $I_{ij}, z_{ij}$ , as a function of the pixel index  $ij$  over an  $N_p \times N_p$  pixel array, for a total of  $2 N_p^2$  unknown parameters. This is a highly under-determined problem with a single image data frame, and we must acquire at least one additional, independent image data frame to render the inverse problem of 3D image reconstruction even marginally solvable. But most images of practical interest are constrained in other ways, e.g., their spatial support extends finitely and both their intensities and depths are smoothly varying from pixel to pixel in both these variables, but still full 3D image construction of an extended object requires, in general, far more image data than needed for point sources.

We have begun computer simulations of 3D scenes with a variety of spatial depth and intensity profiles with image data acquired with the rotating-PSF at two different wavelengths. For the sake of simplicity and to develop a deeper conceptual understanding of the highly complex problem of reconstruction of 3D images from 2D rotating-PSF image data, we chose the two wavelengths  $\lambda_1$  and  $\lambda_2$  to be such that the ratio  $(n_1 - 1)/\lambda_1 : (n_2 - 1)/\lambda_2$  is 1:2, where  $n_1$  and  $n_2$  are the indices of refraction of the spiral glass structure at the two wavelengths. Under this assumption, the ratio of the rates of PSF rotation at the two different  $\lambda$ s can be easily shown to be  $(n_1 - 1)/(n_2 - 1)$ . Also, even if the PSF at  $\lambda_1$  is not invariant under coordinate inversion, as in Fig. 2, it will be invariant under such inversion at  $\lambda_2$  because the analog of the sum (4) representing the PSF at this wavelength has only even- $l$  terms. This property is seen in the double-lobed structure of the PSF displayed in Fig. 7. While both PSFs rotate and keep their shape invariant with changing defocus, their shapes are quite different, and they thus provide the needed PSF diversity for the acquisition of two different image frames. We must assume that the object has the same intensity and depth pattern at the two wavelengths, or at least a simple known correspondence between these patterns at the two wavelengths, so the number of unknowns does not change between the two image frames. Alternatively and more practically, a spatial-light modulator, such as a liquid-crystal array, located either in the aperture plane or a conjugate plane thereof, can create, on demand by means of a voltage modulation, a spiral phase structure of the requisite winding number from zone to zone. This would have the advantage of not relying on any extraneous assumptions that are normally not justified.

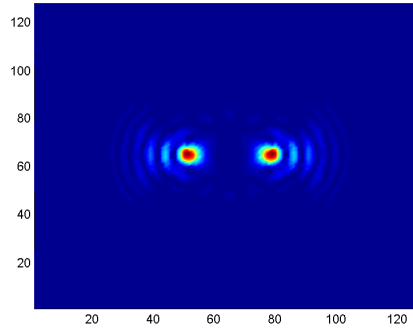


Figure 7: The inversion-symmetric double-lobed structure of the PSF at wavelength  $\lambda_2$ .

## 6 Application to Space Situational Awareness

The robustness of the recovery of the transverse and longitudinal location parameters of closely-spaced point sources along with the increased depth of field afforded by the rotating-PSF imager can be exploited with much advantage in the space-imaging scenario. Let us imagine such an imager situated on a valuable space asset which must, among other tasks, monitor rapidly proliferating space debris of all different sizes and origins [7] for their field locations as well as their ranges away from the asset to initiate any subsequent collision-avoidance maneuvers. The smaller the debris the more numerous they are, with sizes of order  $1mm$  or smaller being about  $10^4$  times more likely than those of order  $1cm$  or larger [8]. The rotating-PSF concept presents a technique for rapid snapshot imaging of a large 3D field of debris and other unfriendly objects.

The maximum depth resolution at sufficiently high values of PSNR corresponds to about 1 radian of defocus phase at the pupil edge,  $\Delta\zeta = 1$ . In view of the definition (3) of  $\zeta$ , this corresponds to a minimum resolvable depth  $\delta z_{min}$  of order

$$\delta z_{min} = \frac{\lambda}{\pi} \left( \frac{l_0}{R} \right)^2, \quad (12)$$

as long as  $\delta z_{min} \ll l_0$ . We note that  $\delta z_{min}$  scales quadratically with range  $l_0$ , but as  $l_0$  becomes so large that  $\delta z_{min}$  becomes comparable to or larger than  $l_0$  then, as the definition (3) suggests,  $\zeta$  becomes independent of  $\delta z$ , and the imager can no longer resolve such large depths. For a telescope diameter of  $2R = 20\text{ cm}$ s and illuminating wavelength of  $\lambda = 1\mu m$ , the minimum resolvable depth at  $l_0 = 1\text{ km}$  is about  $30\text{ m}$  and at  $l_0 = 100\text{ m}$  about  $30\text{ cm}$ , while the operational depth ranges  $\Delta z$  over which the imager produces robust images correspond to  $\zeta$  of order  $2\pi L$ , or 30-50 (for  $L$  5-8) times larger than  $\delta z_{min}$ . These are potentially useful numbers for meaningful space-to-space surveillance applications.

## 7 Conclusions

The work described here presents a detailed theoretical analysis and simulation-based studies of a recently advanced computational imager concept that exploits pupil-phase engineering as a way of encoding depth into PSF rotation. It does so by combining a spiral phase structure with a Fresnel-zone partitioning of the pupil. The PSF generated by such a phase plate merely rotates as a function of the focal depth of the point source.

We have shown that the rotating PSF is just 2-3 times more extended than the clear-aperture PSF, the Airy pattern, while unlike the latter it is highly stable against rapid defocus-dependent spreading. This implies comparable transverse resolution but greatly enhanced depth resolution from single-shot image data taken with the rotating-PSF imager. This allows for a number of current and future SSA applications.



## 8 Acknowledgments

The work reported here was supported by the US Air Force Office of Scientific Research under award numbers FA9550-08-1-0151, FA9550-09-1-0495 and FA9550-11-1-0194.

## References

- [1] E. Dowski, Jr. and W. Cathey, "Extended depth of field through wave-front coding," *Appl. Opt.*, vol. 34, pp. 1859-1866 (1995).
- [2] S. Prasad, "Rotating point spread function via pupil-phase engineering," *Opt. Lett.*, vol. 38, pp. 585-587 (2013).
- [3] S. Pavani and R. Piestun, "High-efficiency rotating point spread functions," *Opt. Express*, vol. 16, pp. 3484-3489 (2008).
- [4] M. Lew, M. Badieirostami, and W. Moerner, "Corkscrew point spread function for far-field three-dimensional nanoscale localization of pointlike objects," *Opt. Lett.*, vol. 36, pp. 202-204 (2011).
- [5] P. Magain, F. Courbin, and S. Sohy, "Deconvolution with Correct Sampling *Astrophys. J.*, v.494, pp.472-476 (1998).
- [6] L. Lucy, "Statistical Limits to Super Resolution," *Astron. Astrophys.*, vol.261, pp. 706-710 (1992)
- [7] H. Klinkrad, *Space Debris - Models and Risk Analysis* (Springer, 2006).
- [8] A. Rossi, "Population models of space debris," *Proc. Intern. Astron. U.*, vol. 2004, pp 427-438 (2004).